Postprocessing workflow of 3D USCT: bridging the gap to the clinic

T. Hopp, M. Zapf, H. Gemmeke, and N.V. Ruiter

Karlsruhe Institute of Technology, Institute for Data Processing and Electronics, Karlsruhe, Germany
E-mail: torsten.hopp@kit.edu

Abstract

As first USCT systems are approaching clinical application, it is an essential task to prepare the reconstructed images for intuitive diagnosis and conform to clinical standards. We describe our post-processing workflow consisting of automated breast segmentation, image fusion, DICOM export and the methods to transfer images to the clinic. The segmentation was tested with 14 images resulting in an average surface deviation of 2.7 mm from semi-automatically segmented images. Modalities were fused applying empiric thresholds for sound speed and attenuation. The exported DICOM files were checked for consistency and tested with open source and commercial DICOM viewers. A teleradiology connection to University Medicine Mannheim was established based on the DICOM e-mail concept. We consider segmentation and image fusion as essential steps for intuitive diagnosis. Using medical standards like DICOM and PACS allows convenient integration into clinical workflows.

Keywords: Image processing, Segmentation, Image fusion, DICOM

1   Introduction

First Ultrasound tomography (USCT) systems are approaching clinical application, e.g. [1, 2]. At Karlsruhe Institute of Technology (KIT) we are developing the world's first full 3D USCT systems, which we are currently testing in clinical trials [3]. Bridging the gap from a purely research system to a clinically applicable system, not only requires the system aspects like fast data acquisition and fast image reconstruction, but also the clinical workflow related aspects in order to prepare the images for intuitive diagnosis, to conform with clinical standards and to seamlessly integrate the new modality into the clinical workflow.
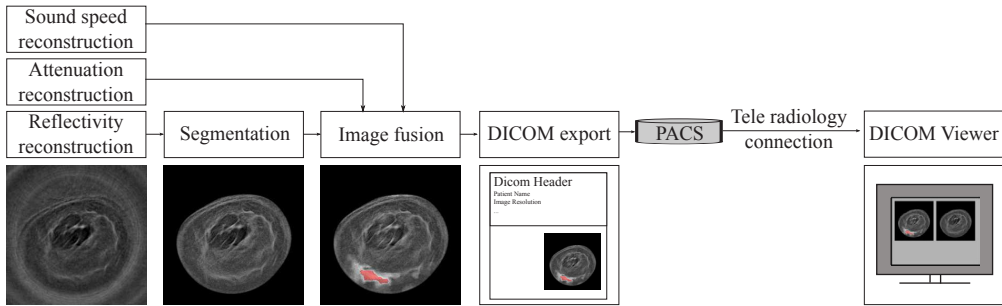
229

Figure 1: Postprocessing workflow of the KIT 3D USCT.

In this paper we describe our post-processing workflow (Figure 1) for USCT images which consists of the following processing steps:

1. Automated segmentation of the breast from the background in order to remove the water background and artifacts outside the breast like aperture reflections.

2. Fusion of the three imaging modalities (reflectivity, sound speed, attenuation) to enable intuitive diagnosis at a glance.

3. Export of the image data into DICOM format to conform with clinical standards.

4. Transfer of image data to the clinic.

2 Methods

2.1 KIT 3D USCT

The KIT 3D USCT consists of a semi-ellipsoidal aperture with a diameter of 26 cm and a depth of 16 cm. The surface of the aperture is equipped with 628 dedicated ultrasound emitters and 1413 receivers which are grouped into 157 transducer array systems (TAS). Approximately spherical waves are emitted by a single ultrasound transducer at a center frequency of 2.5 MHz (approximately 50% bandwidth) while all other receivers acquire the reflected and transmitted signals. Repeating the measurement process for all sender-receiver-combinations results in approximately 890,000 signals, so-called Amplitdue scans (A-scans). Rotational and translational motion of the aperture create further virtual transducer positions to increase the amount of A-scans further. Approximately 10 million A-scans are currently acquired during patient imaging in our clinical studies for one breast volume. From the acquired signal data, transmission volumes are reconstructed using a ray-based algebraic reconstruction technique (ART) [4, 5] and reflection images are reconstructed using Synthetic Aperture Focusing Technique (SAFT) [3].

2.2 Breast segmentation

Though huge datasets with up to 10 million A-scans and 40 GB raw data per breast are acquired, the aperture is still sparse. Due to the sparseness, reflection images typically suffer from grating lobe artifacts, i.e. the water surrounding the breast is not imaged as homogeneous background. For diagnosis and further processing like image registration, volume measurement, etc., segmentation of the breast from the background is essential.

The segmentation problem to be solved is the detection of the breast edge, which appears bright in the reflectivity images due to the change in acoustical impedance between water and skin. We developed an automated breast segmentation [6] based on three-dimensional active contours.

Active contours can be described as an energy minimization problem (equation 1) according to *Kass et al.* [7] as follows:

$$E\left(t_k\right) = w_{int} \int_0^1 E_{int}\left(x\left(s,t_k\right)\right) ds + w_{ext} \int_0^1 E_{ext}\left(x\left(s,t_k\right)\right) \to \min \tag{1}$$

where $x\left(s,t_k\right)$ describes a parametric curve depending on the spatial parameter s and time point t_k, and w_{int} respectively w_{ext} represent weighting factors for the internal energy E_{int} and the external energy E_{ext}. The internal energy describes the smoothness of the parametric curve's geometric shape by introducing an inner tension using the first and second order derivatives. The external energy estimates the proximity of the parametric curve to edges in the image by computing the image gradient at the position of the parametric curve. The minimization problem is tackled by an iterative deformation of the parametric curve based on an Euler-Lagrange modeling [6].

In our formulation we use gradient vector flow (GVF) [8] for computation of the external energy in order to enhance the capture range of contours in the images. As SAFT images depict changes in the impedance we expect high image intensity values at the boundary of the breast, which the method should detect. Consequently we code the intensity information as additional external energy term. Moreover, the 3D USCT aperture characteristics cause a spatially varying contrast of tissue boundaries compared to the water background. Therefore an additional weighting factor is introduced, which depends on the spatial position of the parametric curve. It is determined by the region of interest (ROI) of the 3D USCT, which was previously defined and optimized to produce the optimal illumination, contrast and resolution [9]. The semi-ellipsoidal ROI of the current 3D USCT prototype has dimensions of $10 \times 10 \times 10$ cm. The ROI is modeled by a representation of the ROI in a Gaussian filtered image, which additionally delivers weights on the external force for the parametric curve.

The initial parametric curve has a major influence on the active contour algorithm. For 3D USCT the initial parametric curve is discretized to a three dimensional surface polygon mesh.
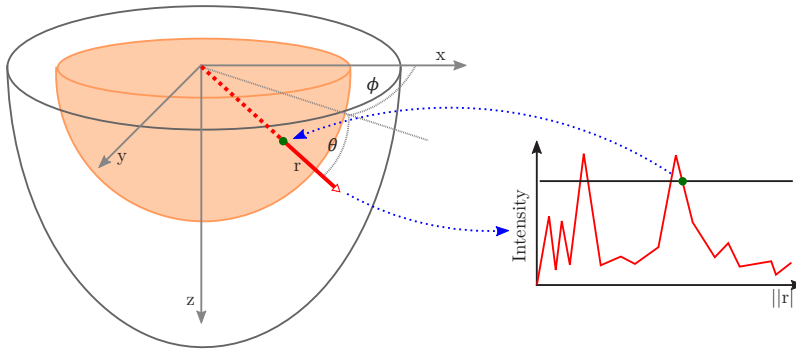
Figure 2: Ray-based detection of the breast surface for initialization of the active contour approach: Along a ray $\vec{r}$ from the center of the USCT aperture intensities are interpolated, resulting in an intensity against radius plot (right). To determine the breast surface reflection, the last occurring intensity peak above a threshold, which is defined by the average intensity of the background, is detected.

Each surface node is generated by a ray based approach as depicted in Figure 2. Image intensities along a ray $\vec{r}$ with elevation angle θ and azimuth angle ϕ and starting at the center of the USCT (red arrow in Figure 2 left) are interpolated from the volume image. Assuming an approximately hemispherical breast shape, the ray thereby intersects the breast boundary approximately normal to the surface. Furthermore assuming that there are no major scattering objects outside the breast, the breast surface is estimated by determining the outermost intensity peak along the ray using a threshold (Figure 2 right). The threshold is chosen by the average intensity of the water background $\bar{I}_{water}$ multiplied with an empirical factor s, which is iteratively decreased from $s = 1.5$ until an intensity value along the ray (I_{ray}) is above the threshold t, i.e. $I_{ray} > t$ with $t = \bar{I}_{water} \cdot s$. The final initial parametric curve is then generated using a polynomial fit to remove outliers from the threshold based surface detection. The purpose is to provide a good first estimate of the position, size and the rough shape of the breast.

The initial parametric curve is iteratively deformed. The iterative process is stopped at a maximum number of iterations, or if the average motion of the parametric curve is smaller than a given tolerance level. The final contour is then used to create a binary segmentation mask which is zero for voxels outside the closed contour. By multiplying the binary segmentation mask voxel-vise with the reconstructed images, the water background can be removed in all three modalities (sound speed, attenuation, reflectivity) as they are imaged in one data acquisition step.

2.3   Image fusion

To facilitate diagnosis we apply an image fusion in order to combine the diagnostic information from all modalities in a single image. The basic idea is to combine high resolution reflectivity images with the quantitative sound speed and attenuation maps. We perform the fusion of two images (sound speed and reflectivity, attenuation and reflectivity) as well as the fusion of all
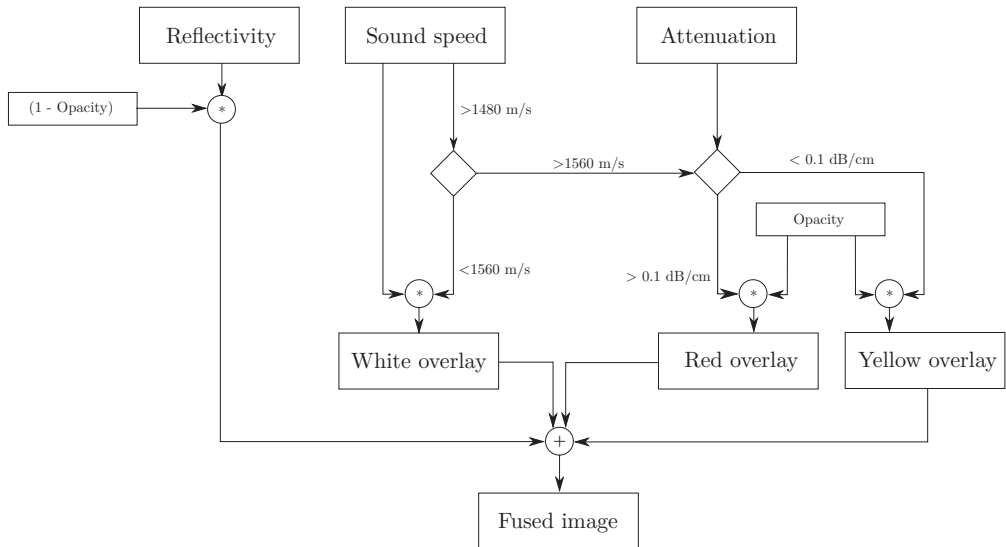
Figure 3: Workflow of the three-modality image fusion, which combines reflectivity with sound speed and attenuation information.

three images. For pair-wise fusion the reflectivity image is rendered as a gray scale background with additional adaption of the contrast by a gray scale windowing. The sound speed map is color-coded in a range between 1300 m/s (blue) to 1600 m/s (dark red). In the same fashion the attenuation map is color-coded in a range between 0 dB/cm (blue) to 1.5 dB/cm (dark red).

To combine all three modalities, several approaches have been proposed, e.g. [10, 11]. Based on our empiric experience with collaborating radiologists we decided to adapt the image fusion developed by *Ranger et al.* [10]. In this method the reflectivity is rendered as gray scale background. An empiric window of sound speed values is used to mask areas with fibroglandular structures and render them overlaid as a cloud like white structure on the reflectivity background. We adapted the method by weighting the opacity of the overlay with the actual sound speed value, i.e. higher sound speeds in the fibroglandular sound speed value window are rendered with less transparency than low sound speed values. Furthermore the method uses a second threshold for the sound speed and a threshold for the attenuation map to mask out a lesion. The attenuation threshold serves as basis to distinguish a benign from a malignant mass. Areas with high sound speeds and high attenuation are therefore rendered as red overlay on the reflectivity background to mark malign lesions, while areas with high sound speed and low attenuation are rendered in yellow to mark benign lesions (Figure 3).

We adapted the thresholds of this method empirically: A sound speed window 1480 m/s to 1560 m/s is used to mask the area of fibroglandular tissue, areas with sound speeds higher than 1560 m/s and attenuation higher than 0.1 dB/cm are considered as malign masses, areas with sound speed higher than 1560 m/s and attenuation lower than 0.1 dB/cm are considered as benign masses.

2.4   Export to DICOM

All segmented and fused images are thereafter exported into the DICOM format, which is a standard for storing and transmitting medical images [12]. DICOM provides a container format which encapsulates the image data together with metadata in a single file. The so-called header holds information about the patient, the image acquisition and image reconstruction. In the KIT 3D USCT case we automatically create the DICOM header by extracting metadata from the data acquisition process (e.g. acquisition date and time, patient position) and the image reconstruction process (e.g. pixel spacing, modality type, windowing levels). The volume dataset is split into slices according to a user selected slicing direction (coronal, transversal, sagittal). Each slice is exported to a single DICOM file without data compression. In case of fused images, the photometric interpretation header tag is set to RGB and the RGB values are exported accordingly.

DICOM uses Information Object Definitions (IOD) to define a standard set of header tags required for certain imaging modalities to conform with the standard. As currently no IOD for USCT images is defined in the DICOM standard, we apply the CT IOD and fill header tags with pseudo values if needed.

The DICOM files are created using the MATLAB image processing toolbox. To evaluate the conformity with the DICOM standard, the exported files are checked with the DICOM validator software "dciodvfy" by *D.A. Clunie* [13]. Visual inspection of the images is carried out using the DICOM viewer RadiAnt [14].

2.5   Data transfer to the clinic

As the image reconstruction for our 3D USCT prototype is in our current clinical study performed on a multi-GPU system at KIT, resulting images need to be transferred to the clinic in order to evaluate the diagnostic information in a concordance study in comparison to MRI. For this purpose we apply the established teleradiology transfer of the clinic. For our current clinical study, the transfer method is based on DICOM e-mails [15]. The architecture of the data exchange infrastructure is depicted in Figure 4. v

After DICOM export the files are automatically send to a local Picture Archiving and Communication System (PACS) using the DICOM Toolkit (DCMTK). We use an installation of the public domain Conquest DICOM software [17] as PACS. From the PACS a data transfer can be triggered. On transfer request the DKON3 software provided by University Medicine Mannheim encrypts the DICOM files using Pretty Good Privacy (PGP), attaches them to an e-mail and sends the e-mail via a mail server to the destination mail server [15]. On the receiver site the e-mail attachments are decrypted and images are sent to the clinic PACS, from which they can be accessed from DICOM viewer workstations.
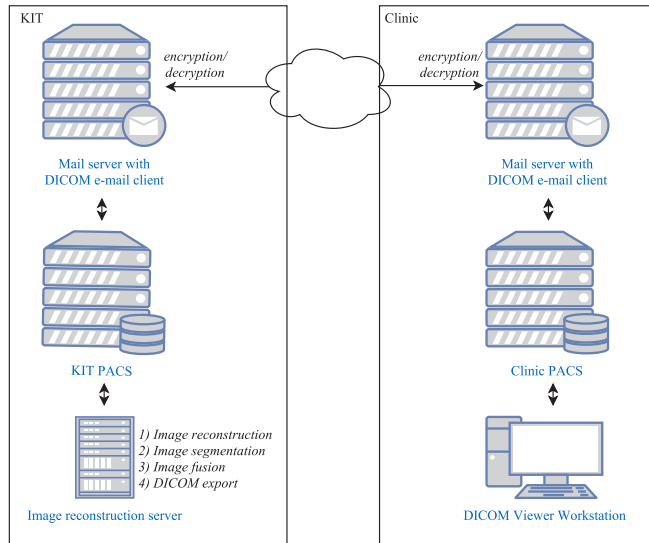
Figure 4: Architecture of the DICOM infrastructure for data transfer to the clinic. At KIT images are reconstructed, segmented, fused and exported to DICOM in a reconstruction server, which send the images to a local PACS. To transfer the data to the clinic, encrypted DICOM e-mails are sent to the destination where they are decrypted and images are transferred to the clinic PACS.

3 Results

The breast segmentation was tested with 14 images from 9 patients. Images were reconstructed with an isotropic pixel resolution of $(0.74 \, mm)^3$. A semi-automated segmentation based on edge detection, manual corrections and three-dimensional surface fitting as described in our earlier publication [18] served as ground truth for evaluation. The deviation of both segmented breast surfaces was determined by calculating the mean three-dimensional Euclidean distance of the surface nodes of the active contour to the closest surface voxels of the semi-automated segmentation and vice versa. Both measurements were averaged to get the final deviation metric. Applying our model-based initialization and the traditional active contour approach with GVF but without including USCT aperture characteristics, the average of mean surface distance was 3.2 mm (standard deviation $\pm 1.3 \, mm$). By including the USCT aperture characteristics the average of mean surface distances was $2.7 \, mm$ ($\pm 1.1 \, mm$). These experiments were conducted with a constant initial parameter set.
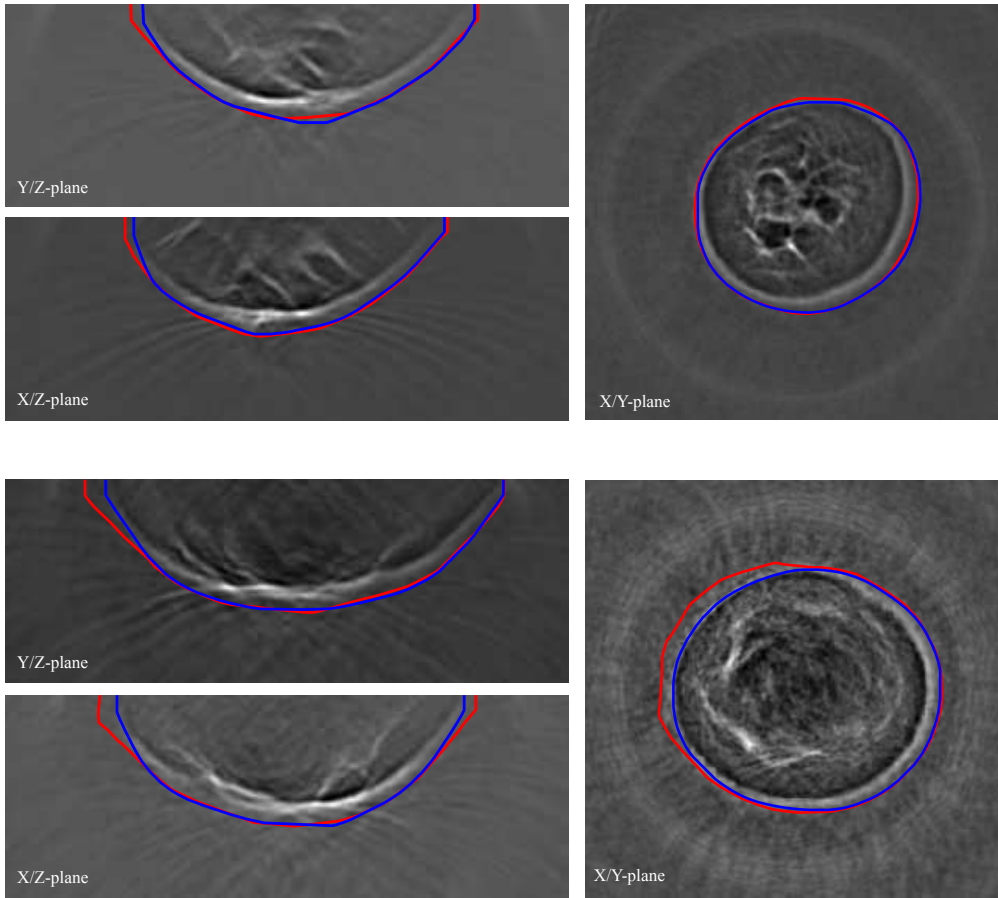
Figure 5: Segmentation result of a patient volume. The blue outline shows the semi-automated segmentation which serves as ground truth for evaluation, the red outline shows the result of the fully automated segmentation. Top images: patient volume reconstructed from signals at ten aperture positions with an average surface deviation of $0.9\,mm$. Bottom images: patient volume reconstructed from signal at four aperture positions with an average surface deviation of $1.5\,mm$
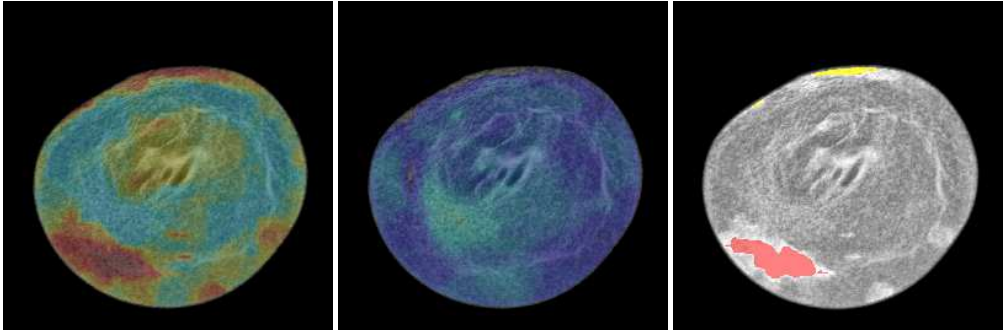
Figure 6: Results for the image fusion methods, from left to right: combination of reflectivity and sound speed, combination of reflectivity and attenuation, combination of all three modalities.

Figures 5 shows segmentation results with patient data. The largest segmentation errors could be observed close to the top of the USCT aperture (Figure 5, top in each image on the left), where the contrast of the breast against the background is decreased significantly due to the aperture geometry. It appeared that varying the threshold for the contour initialization had a major influence on the results. To demonstrate the influence, we changed the threshold parameter once to a different empiric constant for all datasets and manually selected for each dataset the more accurate segmentation. Thereby the average surface distance further decreased to $2.2\,mm\,(\pm 1.3\,mm)$.

After image fusion with the method described above (Figure 6), the images of our first clinical study with 10 patients were successfully exported to DICOM. The DICOM validation successfully tested the header attributes against the requirements of the IOD, the encoding of data elements, the data element value representation against the DICOM data dictionary and the consistency of attributes.

The PACS installation was tested successfully by automatically transferring the exported DICOM files via DCMTK. The PACS currently holds the anonymized image data of the 10 patients imaged in our first clinical study as well as image data of phantoms imaged with KIT 3D USCT. It is constantly growing by adding the image data of our ongoing second clinical study. The PACS can be accessed at KIT with any DICOM viewer after obtaining appropriate authorization. A visual representation of an exemplary DICOM viewer connected to the local PACS system is given in Figure 7. The images are correctly represented and can be viewed side-by-side with according MRI images. The dialog in Figure 7 (right) shows the attached metadata in the DICOM header.

A teleradiology connection to University Medicine Mannheim was established based on the DICOM e-mail concept and successfully tested by transferring images from KIT to the University Medicine Mannheim and vice versa.
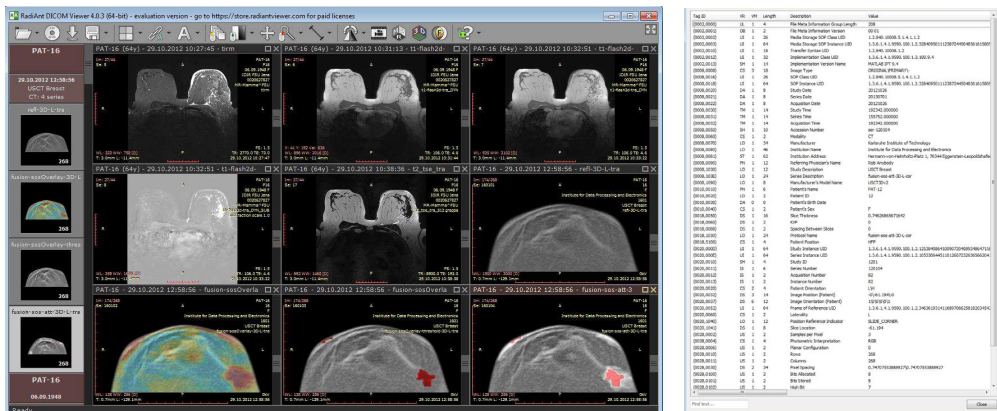
237

Figure 7: Visual inspection of the exported DICOM files using the RadiAnt DICOM viewer. Left: side-by-side view of USCT images with MR images of the same patient. Right: screenshot of the DICOM header dialog, which provides the attached metadata for a USCT image.

4   Discussion and conclusion

We successfully established a fully automated post-processing workflow to bring 3D USCT closer to clinical application. We consider segmentation and image fusion as an essential steps for intuitive diagnosis which is focused to the most relevant clinical information.

The accuracy achieved with our fully automated segmentation is comparable to a semi-automated segmentation with an average surface deviation of $2.7\,mm$. Based on the successful application to patient data we believe that the segmentation is robust against clinical variability of the imaging process and different anatomies of the breast. To proof this we are planning to extend the evaluation to a larger patient cohort, which will be recruited during our ongoing clinical study.

Using medical standards like DICOM and PACS will allow an easy integration into clinical workflows. By applying the validation software we ensure that the exported DICOM files follow the DICOM standard as close as possible. Yet due to the lack of an appropriate IOD, some header tags have to be filled with pseudo values. This might cause confusion with some DICOM viewer software if the DICOM header is not properly interpreted. In future we propose to extend the DICOM standard by a dedicated IOD fulfilling the metadata requirements of USCT.

In conclusion we believe that the presented work provides essential steps to integrate USCT into clinical workflows, and to establish the imaging method for clinical applicability.

References

[1]   N. Duric, P. Littrup, P. Chandiwala-Mody, C. Li, S. Schmidt, L. Myc, O. Rama, L. Bey-Knight, J. Lupinacci, B. Ranger, A. Szczepanski, E. West: In-vivo imaging results with ultrasound tomography: Report on an ongoing study at the Karmanos Cancer Institute. Proc. SPIE Medical Imaging 7629 (2010), 76290M

[2]   J. Wiskin, D. Borup, S. Johnson, M. Berggren, D. Robinson, J. Smith, J. Chen, Y. Parisky, J. Klock: Inverse Scattering and Refraction Corrected Reflection for Breast Cancer Imaging Proc. SPIE Medical Imaging 7629 (2010) 76290K

[3]   N. Ruiter, M. Zapf, R. Dapp, T. Hopp, W. Kaiser, H. Gemmeke: First Results of Clinical Study with 3D Ultrasound Computer Tomography. Proc. IEEE Ultrasonics Symposium (2013), 651654

[4]   R. Dapp, M. Zapf, N. V. Ruiter: Geometry-independent speed of sound reconstruction for 3D USCT using apriori information. Proc. IEEE Ultrasonics Symposium (2011), 14031406

[5]   R. Dapp, H. Gemmeke, N. V. Ruiter: Attenuation reconstruction for 3D Ultrasound Computer Tomography. Proc. 19th International Conference on Systems, Signals and Image Processing (IWSSIP) (2012), 484487

[6]   T. Hopp, W. You, M. Zapf, W.Y. Tan, H. Gemmeke, N.V. Ruiter: Automated breast segmentation in ultrasound computer tomography SAFT images, Proc. SPIE Medical Imaging 10139 (2017), 101390G

[7]   M. Kass, A. Witkin, D. Terzopoulos: Snakes: Active contour models. International Journal of Computer Vision, 1(4), (1988), 321331

[8]   C. Xu, J.L. Prince: Snakes, Shapes, and Gradient Vector Flow. IEEE Transactions on Image Processing, 7(3), (1998), 359369

[9]   G.F. Schwarzenberg, M. Zapf, N.V. Ruiter: Aperture Optimization for 3D Ultrasound Computer Tomography. Proc. IEEE Ultrasonics Symposium (2007), 1820-1823

[10]   B. Ranger, P. Littrup, N. Duric, P. Chandiwala-Mody, C. Li, S. Schmidt, J. Lupinacci: Breast ultrasound tomography versus MRI for clinical display of anatomy and tumor rendering: preliminary results. American Journal of Roentgenology, 198(1) (2012), 233239

[11]   T. Hopp, M. Zapf, E. Kretzek, J. Henrich, A. Tukalo, H. Gemmeke, C. Kaiser, J. Knaudt, N.V. Ruiter: 3D Ultrasound Computer Tomography: Update from a clinical study. Proc. SPIE Medical Imaging 9790 (2017), 97909

[12]   NEMA PS3 / ISO 12052, Digital Imaging and Communications in Medicine (DICOM) Standard, National Electrical Manufacturers Association, Rosslyn, VA, USA (available free at http://medical.nema.org/)

[13]   D.A. Clunie: DICOM Validator - dciodvfy, available online at http://www.dclunie.com/dicom3tools/dciodvfy.html

[14]   Medixant: RadiAnt DICOM Viewer, available online at https://www.radiantviewer.com/

[15]   G. Weisser, U. Engelmann, S. Ruggiero, A. Runa, A. Schrter, S. Baur, M. Walz: Teleradiology applications with DICOM-e-mail. European Radiology 17 (2007), 1331-1340.

[16]   The OFFIS computer science institute: DCMTK - DICOM Toolkit, available online at
       http://dicom.offis.de/dcmtk.php.en

[17]   M. van Kerk, L. Zijp: Conquest DICOM software. Netherlands Cancer Institute. avail-
       able online at https://ingenium.home.xs4all.nl/dicom.html.

[18]   T. Hopp, M. Zapf, N.V. Ruiter: Segmentation of 3D Ultrasound Computer Tomogra-
       phy Reflection Images using Edge Detection and Surface Fitting, Proc. SPIE Medical
       Imaging 9040 (2014), 904066